IOPscience iopscience.iop.org

Home Search Collections Journals About Contact us My IOPscience

Design, fabrication and actuation of a MEMS-based image stabilizer for photographic cell phone applications

This content has been downloaded from IOPscience. Please scroll down to see the full text.

2010 J. Micromech. Microeng. 20 075025

(http://iopscience.iop.org/0960-1317/20/7/075025)

View the table of contents for this issue, or go to the journal homepage for more

Download details:

IP Address: 140.113.38.11

This content was downloaded on 25/04/2014 at 03:26

Please note that terms and conditions apply.

J. Micromech. Microeng. **20** (2010) 075025 (11pp) doi:10.1088/0960-1317/20/7/075025

Design, fabrication and actuation of a MEMS-based image stabilizer for photographic cell phone applications

Jin-Chern Chiou[1,2], **Chen-Chun Hung**[1] **and Chun-Ying Lin**[1]

[1] Institute of Electrical and Control Engineering, National Chiao Tung University, Hsin-Chu, Taiwan, Republic of China

[2] School of Medicine, China Medical University, Taichung, Taiwan, Republic of China

E-mail: chiou@mail.nctu.edu.tw, hungin.ece92g@nctu.edu.tw and sikun.ece95g@nctu.edu.tw

Received 11 December 2009, in final form 11 May 2010
Published 11 June 2010
Online at stacks.iop.org/JMM/20/075025

Abstract

This work presents a MEMS-based image stabilizer applied for anti-shaking function in photographic cell phones. The proposed stabilizer is designed as a two-axis decoupling *XY* stage $1.4 \times 1.4 \times 0.1$ mm^3 in size, and adequately strong to suspend an image sensor for anti-shaking photographic function. This stabilizer is fabricated by complex fabrication processes, including inductively coupled plasma (ICP) processes and flip-chip bonding technique. Based on the special designs of a hollow handle layer and a corresponding wire-bonding assisted holder, electrical signals of the suspended image sensor can be successfully sent out with 32 signal springs without incurring damage during wire-bonding packaging. The longest calculated traveling distance of the stabilizer is 25 μm which is sufficient to resolve the anti-shaking problem in a three-megapixel image sensor. Accordingly, the applied voltage for the 25 μm moving distance is 38 V. Moreover, the resonant frequency of the actuating device with the image sensor is 1.123 kHz.

(Some figures in this article are in colour only in the electronic version)

1. Introduction

In this work, the feasibility of a variety of applications of a MEMS-based (micro-electro-mechanical system) *XY* stage has been studied. Additionally, the stage has been manufactured using the micro/nano fabrication process based on the advantages of device miniaturization to realize highly precise systems [1]. In terms of the driving function of the MEMS-based *XY* stage, a comb-drive actuator has a very important role in optical applications [2–7] and the probe positioning system [8] because it is easily controlled, and has highly precise position control and low power consumption. The electrostatic *XY* stage has been widely applied for scanning probe microscopy (SPM) probes [9, 10], data storage [11–13] and nano-position control [1, 14–16].

The photographic function has an increasingly significant role in cell phone applications. Due to consumer demand for an increased number of pixels, many novel photographic functions such as digital single-lens-reflex (DSLR) are embedded in commercial cell phones. Anti-shake technology is among the many new technologies developed for mobile phones. An increase in the number of pixels has increased undesirable image blurring caused by a photographer's shaking hands. The image stabilization function is a popular solution that resolves this problem [17]. Among the familiar image stabilization techniques are lens shifting [18], charge coupled device (CCD) shifting [19] and signal processing [20]. Signal processing is a conventional anti-shaking technique used in mobile phones. Although signal processing requires no additional hardware and does not interfere with system module miniaturization, reliable performance depends markedly on the algorithm used. Given the demand for device miniaturization, the lens-shifting anti-shaking approach is insufficient as adding a movable lens causes nonlinearity in control that must be compensated for by a complex control algorithm. Although the method of CCD-shifting requires an actuating system associated with the image sensor, image sensor shifting does not adversely affect

 © 2010 IOP Publishing Ltd Printed in the UK & the USA

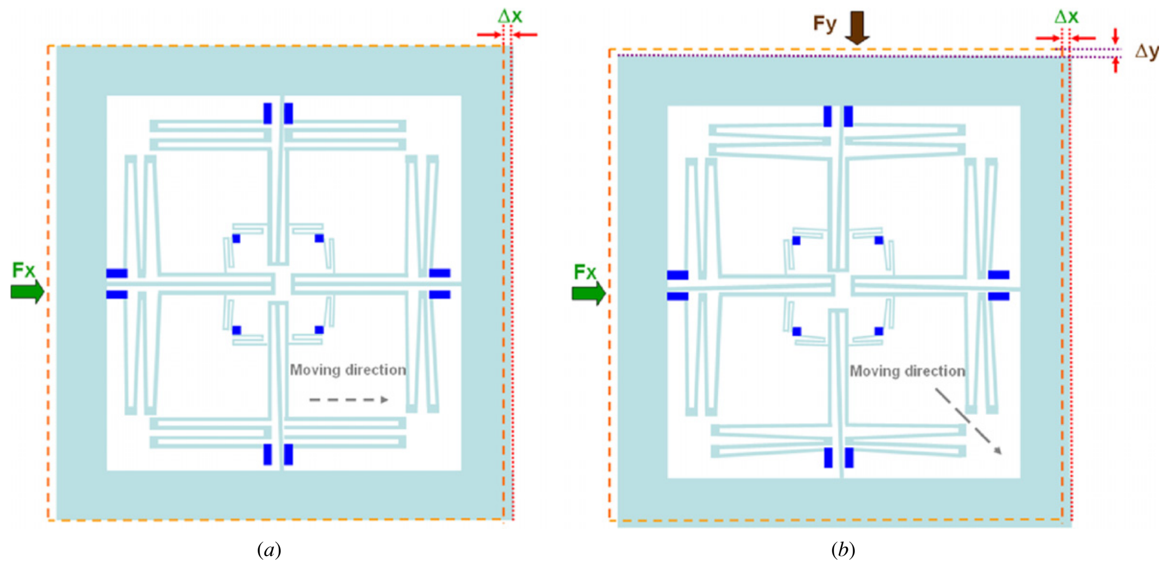

(*a*) (*b*)

Figure 1. Illustration of driving modes of the decoupling *XY* stage: (*a*) in the *X*-direction only and (*b*) in both *X*- and *Y*-directions.

miniaturization. Additionally, system slimming is better than the lens-shifting method [17]. Suspended microstructures in a MEMS device can be moved precisely and integrated with microelectronic circuits monolithically on a chip [21]. The *XY* stage with the CCD-shifting method is appropriate as an image stabilizer to miniaturize the camera module in cell phones. This work describes a novel MEMS-based two-dimensional (2D) decoupling actuator that functions as an image stabilizer in the CCD-shifting stage. The main goal of this research is to identify a new fabrication process that downscales the image stabilizer in existing cameras that can be used in portable photographic devices such cell phones and watches. The design of a MEMS-based image stabilizer that is suitable for cell phones with a three-megapixel camera requires an actuator that can move at least 25 μm away from the structure [17], has a sufficiently strong structure that can withstand the load of a 6.36 × 6.24 × 0.1 mm^3 image sensor and is decoupled in two dimensions when driven in a single direction or in two directions. Therefore, a structure with a high aspect ratio and 100 μm thick silicon springs and comb fingers is designed. Four decoupling springs are the main suspended and decoupling structures bonded onto a three-megapixel image sensor. This device is manufactured using a special Si-based anisotropic etching process that includes double-side lithography, three inductively coupled plasma (ICP) etching processes and flip-chip bonding. This actuator is designed as an image stabilizer that has the same weight as a 6.36 × 6.24 mm^2 three-megapixel image sensor. Considering the electrical connections in an image sensor, 32 decoupling signal springs are used as the output routing. Based on the design of a wire-bonding assistive holder (WBAH), the image sensor can bond with the suspended image stabilizer and with a 32-signal output stage. The 25 μm displacement is achieved when driven in a moving direction with a 45 dc voltage and an excellent vertical decoupling effect occurs.

2. Concept and structure design

The proposed MEMS-based image stabilizer focuses on designing a 2D decoupling actuator that can carry a three-megapixel image stabilizer that compensates for image blurring caused by shaking hands while taking a photograph. The design of the *XY* stage is as follows.

2.1. Structure design of the XY stage

The proposed image stabilizer is designed to achieve an excellent decoupling effect with a suitable device size for suspending the image sensor while considering the signal output. To achieve the anti-shaking function, this device must be designed to have a decoupling structure that compensates for pixels blurred by shaking hands without an additional deviation in another direction. Figure 1(*a*) shows a simple schematic diagram of the proposed decoupling structure. When a force $\boldsymbol{F_x}$ acts in a single-direction decoupling structure, only a displacement $\Delta \boldsymbol{x}$ occurs, which is parallel to the driving force, and is almost without additional displacement in another direction. Figure 3(*b*) shows a simplified diagram of the operation of the proposed decoupling *XY* stage when different forces are applied in the *x*- and *y*-directions. According to the decoupling design, displacements in the *x*- and *y*-directions are Δx and Δy, respectively, with perfect mechanical isolation between the two orthogonal driving directions. The proposed design differs from that of the familiar single-crystal silicon symmetrical and decoupled (SYMDC) micro gyroscope structure [22] in terms of anchor location. The inner anchor conceals the device driving part under the image sensor and effectively reduces device size such that it can be implanted into cell phones.

To suspend a 6.36 × 6.24 × 0.1 mm^3 image sensor, the actuator is designed and fabricated with a device thickness of 100 μm, accompanied by a large stiffness effect between the *z*-direction and the *x*- or *y*-directions separately. For the image sensor signal output, circuit routing must be patterned

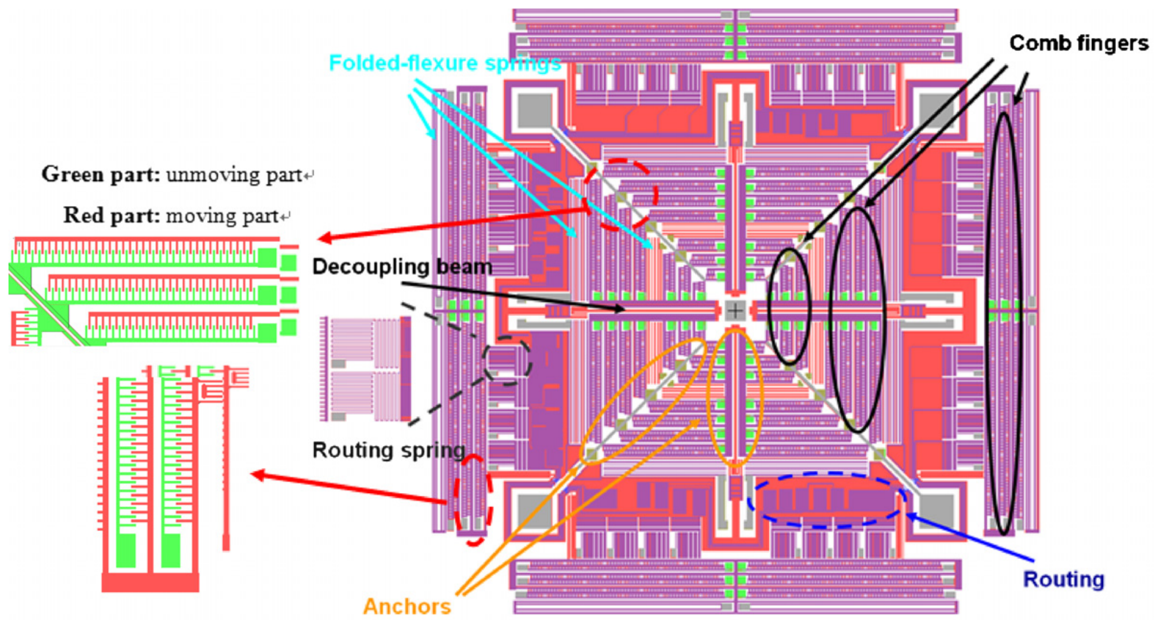

Figure 2. Structure design of the *XY* stage.

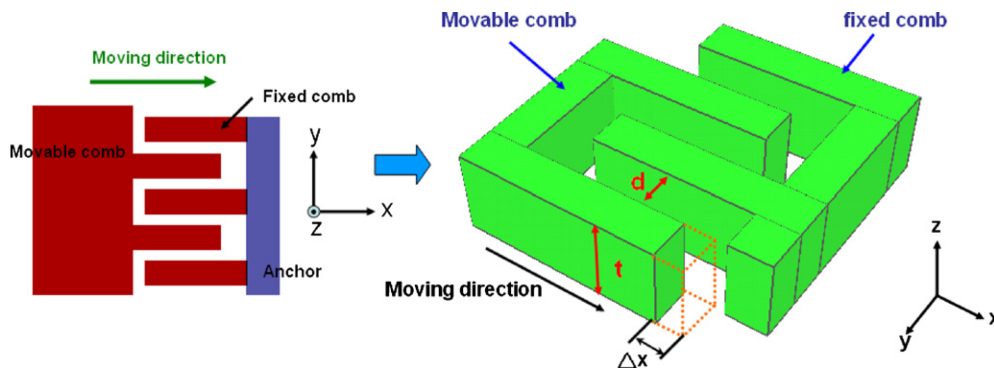

Figure 3. Schematic of the comb finger pair.

on the device layer. The design of the signal routing springs and pads ensures that the electrical connections are working. The routing springs and intermediary pad design have an electrical connection with cell phone circuits by bonding twice from the image sensor pad to the electrical routing pad and from the electrical routing pad to the PCB output pad. Figure 2 schematically depicts the design of the entire device. According to this kinematic design (figure 1), one primary decoupling beam and three pairs of folded springs of various sizes are designed separately in each direction to satisfy decoupling requirements. The designed inner comb finger pairs and anchors miniaturize the device such that it can be embedded in a cell phone. The outer comb-driven finger pairs are designed as assisted driving components to reduce driving voltage for circuit integration in a cell phone module. The outer comb-driven assisted finger pairs are connected to the main structure by four folded springs. All comb-driven actuators are designed in a pull-only driving manner and are located in the *X*+, *X*−, *Y*+ and *Y*− directions individually. To design symmetrical springs, electrical routings must have a balanced layout as well as eight signal output springs and pads in each direction. The signal output springs are as thin as possible to ensure that they have a small stiffness value with a minimal impact on the entire spring. The electrical potentials between the structure and signal output are separated due to the design of the isolation layers and contact windows.

2.2. *Operating principles of the electrostatic comb-drive actuator*

The proposed image stabilizer is driven by electrostatic forces. Figure 3 shows a simple schematic diagram of the comb-driven model [23]. When voltage is supplied, electrostatic force $\boldsymbol{F}$ is generated; the formula for the relationship between the driving force and attached voltage can be expressed as

$$F = \frac{1}{2}\frac{\partial C}{\partial x}V^2 = \frac{nt\varepsilon_o\varepsilon_r V^2}{d}, \tag{1}$$

where C is the capacitance between the stator and the rotor, V is the applied electrical potential, d is the gap displacement, t is the thickness, n is the number of fingers, ε_r is relative permittivity and ε_o is permittivity in air. For simplicity, we assume that the image stabilizer follows Hooke's law;

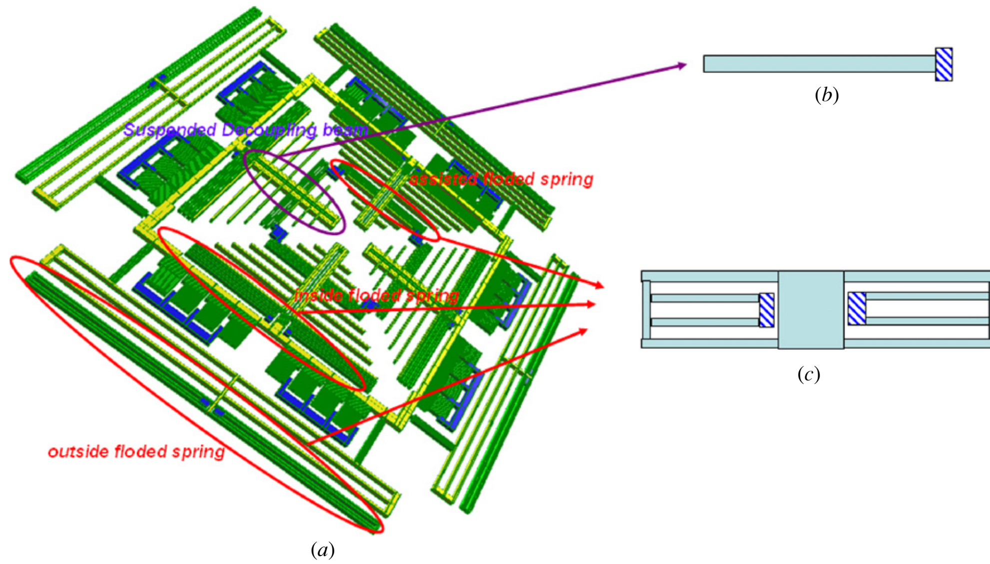

Figure 4. Illustrations of (*a*) decoupling structures, (*b*) decoupling flexure beams and (*c*) folded flexure beams.

therefore, the force F_s is supplied along the *x*-direction and the related equation is

$$F_s = k_{x\text{-system}} x, \tag{2}$$

where $k_{x-\text{system}}$ is the equivalent spring stiffness in the *x*-direction and *x* is the moving displacement. Integrating equations (1) and (2) yields equation (3):

$$x = \frac{1}{2}\frac{nt\varepsilon_o\varepsilon_r V^2}{dk_{x\text{-system}}} \tag{3}$$

Via equation (3), one can maximize the thickness/gap aspect ratio of the comb structure and minimize the gap and $k_{x-\text{system}}$.

2.3. Design and estimation of spring stiffness

The proposed *XY* stage has several suspension beams (figure 4(*a*)). Based on the main actuating device, the decoupling beams and suspension beams are respectively designed as flexure beams and folded beams. Figure 4(*a*) schematically depicts the decoupling and suspended structures. The suspension beams are composed of outside folded beams, inside folded beams, and inside-assisted folded beams. Figure 4 schematically depicts the suspended structures. In considering the decoupling flexure beams (figure 4(*b*)), stiffness in the lateral and axis directions can be expressed as

$$\begin{aligned} k_{x\text{ decoupling beam}} &= \frac{E_d h_d b_d^3}{L_d^3} \\ k_{y\text{ decoupling beam}} &= \frac{E_d h_d b_d}{L_d}, \end{aligned} \tag{4}$$

where $k_{x\text{ decoupling beam}}$ and $k_{y\text{ decoupling beam}}$ are the stiffness of the decoupling beam in the lateral direction and axis direction, respectively, E_d is Young's modulus of the decoupling flexure beam and L_d, b_d and h_d are the length, width and thickness of the decoupling flexure beam, respectively. The stiffness ratio of the decoupling beams can be expressed as

$$K_D = \left|\frac{k_{y\text{ decoupling beam}}}{k_{x\text{ decoupling beam}}}\right| = \left(\frac{L_d}{b_d}\right)^2. \tag{5}$$

Figure 4(*c*) schematically depicts the folded flexure beam. The stiffness of a folded beam in the lateral direction, $k_{x\text{ folded beam}}$, and its axial direction, $k_{y\text{ folded beam}}$, was obtained by Legtenberg *et al* [24] as follows:

$$\begin{aligned} k_{x\text{ folded beam}} &= \frac{2E_f h_f b_f}{L_f} \\ k_{y\text{ folded beam}} &= \frac{2E_f h_f b_f^3}{L^3}, \end{aligned} \tag{6}$$

where $k_{x\text{ folded beam}}$ and $k_{y\text{ folded beam}}$ are the stiffness of the folded flexure beam in the lateral direction and axis direction, respectively; E_f is Young's modulus of the decoupling flexure beam; and L_f, b_f and h_f are the length, width and thickness of the decoupling flexure beam, respectively. The stiffness ratio of the folded beams can be expressed as

$$K_F = \left|\frac{k_{y\text{ folded beam}}}{k_{x\text{ folded beam}}}\right| = \left(\frac{L_f}{b_f}\right)^2. \tag{7}$$

The total stiffness of the main suspension beam of the *XY* stage in the *x*- and *y*-directions can be expressed as

$$\begin{aligned} k_{x\text{ system}} &= 2k_{x\text{ decoupling beam}} + 2k_{x\text{ outside folded beam}} \\ &\quad + 2k_{x\text{ inside folded beam}} + 2k_{x\text{ inside assisted folded beam}} \\ k_{y\text{ system}} &= 2k_{y\text{ decoupling beam}} + 2k_{y\text{ outside folded beam}} \\ &\quad + 2k_{y\text{ inside folded beam}} + 2k_{y\text{ inside assisted folded beam}} \end{aligned} \tag{8}$$

Additionally, the stiffness ratio of the proposed image stabilizer can be expressed as

Table 1. Specifications of the image stabilizer.

Specification	Value
Device size (mm^2)	14 × 14
Image sensor size (mm^2)	6.36 × 6.64
Structure layer thickness (μm)	120
Gap of finger pair (μm)	10
Number of comb finger pairs	1020
Width of the folded spring (μm)	15
Length of the outside folded spring (μm)	4000
Width of the outside folded spring (μm)	20
Length of the inside folded spring (μm)	2280
Width of the inside folded spring (μm)	12
Length of the inside assisted folded spring (μm)	1200
Width of the inside assisted folded spring (μm)	14
Length of suspended decoupling beams (μm)	2700
Width of suspended decoupling beams (μm)	26

$$K_{\text{system}} = \left|\frac{k_{x\text{system}}}{k_{y\text{ system}}}\right| = |\{2k_{x\text{ decoupling beam}} + 2k_{x\text{ outside folded beam}} + 2k_{x\text{ inside folded beam}} + 2k_{x\text{ inside–assisted folded beam}}\}/\{2k_{y\text{ decoupling beam}} + 2k_{y\text{ outside folded beam}} + 2k_{y\text{ inside folded beam}} + 2k_{y\text{ inside–assisted folded beam}}\}| \tag{9}$$

According to the specifications of the proposed image stabilizer (table 1), the system stiffness ratio of the proposed image stabilizer can be determined and simulated as 2.12 × 10^6.

2.4. Design and evaluation of range of motion of the decoupling XY stage

Most commercially available photographic cell phones have a camera with a capacity of two or three megapixels, but lack an anti-shaking function. Notably, small movements while taking a picture cause image blurring. Figure 5 shows the relationship between the number of blurred pixels and the angle of shaking hands. When a camera moves through an angle dθ on the horizontal plane, the number of blurred pixels can be represented as

$$BP = \frac{\mathrm{d}\theta}{\theta_L} P_H, \tag{10}$$

where θ_L is the horizontal angle and P_H is the total number of horizontal blurred pixels. Low-cost cameras typically have an angular field of view of 35–45°. When individuals take pictures using a camera with a three-megapixel image sensor and a 45° field of view [25], experimental results indicate that a maximum horizontal drift of 0.08° occurs in 2 s when hands are shaking. This work adopts the Micron MT9T012 image sensor with three megapixels (2056 × 1544 pixels); the image sensor is bonded to the designed device. From equation (10), each pixel corresponds to a horizontal angle of 0.022°. Therefore, the number of horizontal blurred pixels is approximately 3.7. Since each pixel of the MT9T012 image sensor is 2.2 × 2.2 μm^2, the *XY* stage must have a range of motion of at least 8.14 μm to facilitate the adjustment of a blurred image. Given

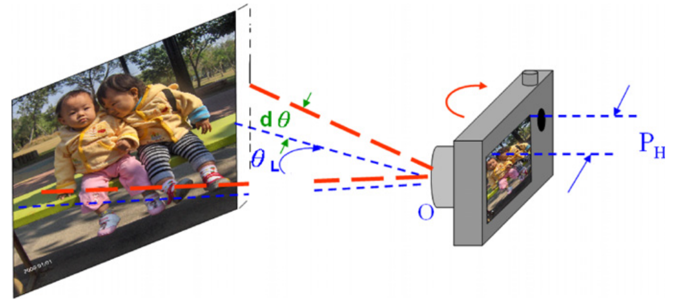

Figure 5. Illustrations of the relation between the blur pixel and hand shaking angle.

that many commercially available cameras have ×3 zoom-in and zoom-out functions, the range of motion must be three times greater than 24.42 μm. The anti-shaking function requires a moving range in the vertical direction of a driven force of <2.2 μm (1 pixel size). This finding implies that the decoupling ratio of the *x* displacement to the *y* displacement must exceed 11.1.

3. System modeling and FEA simulation

This work elucidates and models the decoupling effect, stiffness and natural frequency of the proposed image stabilizer by developing and simulating a decoupling actuator using IntelliSuite 8.2. During static simulation, this software simulates the moving distance in plane and the coupled mechanical interference of the image stabilizer in each orthogonal direction. During dynamic simulation, this software simulates resonant frequency.

3.1. Simulation of the decoupled main structure of the proposed image stabilizer

This section describes the design and simulation of the decoupling structure. Due to the complexity in simulating the entire device, the decoupling effect is simulated using a simplified framework of the *XY* stage, the mechanical mesh size is 15 μm at each decoupling and folded beam in the *XY* plane and the meshing size is 20 μm in the *z*-axis. The total number of element nodes is 265 080. Figure 6 shows simulation results.

Notably, non-decoupling structures are excluded. Four major decoupling springs are designed inside the main structure and combined with the hidden driving comb finger pairs. The decoupling effect of the main structure is simulated based on the following actual boundary conditions: (1) the anchors and stators are ignored since they are bonded with a substrate and do not influence simulation results; (2) the shuttle, decoupling beams and flexure beams are suspended above the substrate, such that the parts can move freely. When the simple models of the designed moving spring and a frame-loaded spring are the same size as that of the image stabilizer, an obvious decoupling effect occurs in the *x*- and *y*-directions (figures 6(*a*) and (*b*)). During simulation, a specific force F_y is applied in the *y*-direction, resulting in a 30 μm displacement in the *y*-direction. Simulation results indicate that a moving

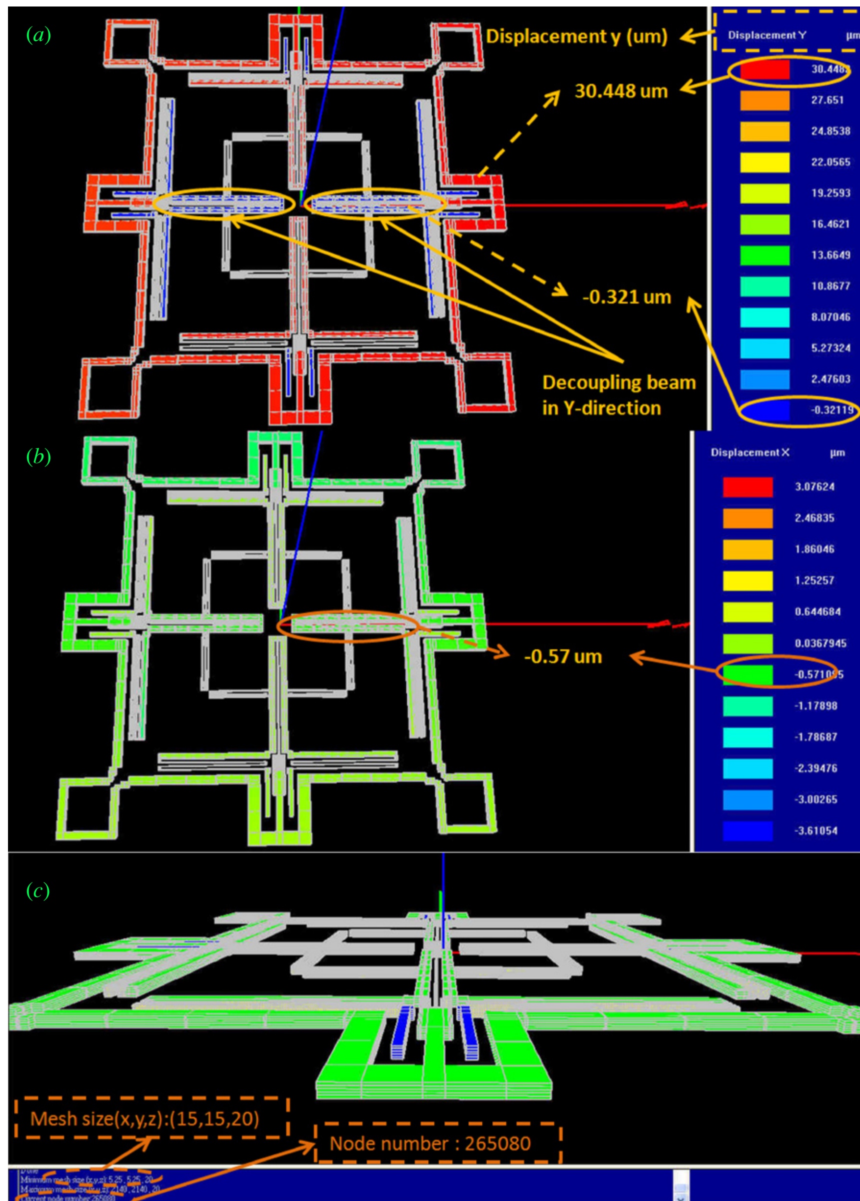

Figure 6. Schematic of decoupling simulation in (*a*) the *Y*-direction and (*b*) the *X*-direction when the main structure of the image stabilizer is driven with outside force in the *Y*-direction. (*c*) Mesh size and node number after mechanical meshing.

displacement of only 0.55 μm occurs in the *x*-direction. The simulated decoupling ratio of the *y* displacement to the *x* displacement indicates that the decoupling effect is excellent in the movable springs, and is significantly greater than that required for decoupling.

3.2. Simulation of resonant frequency of the proposed image stabilizer

The vibration characteristics are verified when the *XY* stage is under dynamic loading by performing instantaneous analysis using the finite element method (FEM) software IntelliSuite 8.2 to determine resonant frequency and model shapes of the proposed structure. In this simulation, the spring structures are completely reserved, and the weights of the *XY* stage and image sensor are calculated and are equivalent to those of the other structures. Equation (11) derives resonant frequency:

$$F_{\text{resonant}} = \frac{1}{2\pi}\sqrt{\frac{k}{M}}, \tag{11}$$

where $\boldsymbol{k}$ is system stiffness of the image stabilizer, $\boldsymbol{M}$ is overall weight of the image stabilizer and $\boldsymbol{F}_{\text{resonant}}$ is the resonant frequency of the image stabilizer.

The simulated resonant frequency in the first mode is 1130.1 Hz and movement is in the *x*-direction; that of the second mode is 1213.1 Hz with movement in the *y*-direction and that of the third mode is 1353.52 Hz, which rotates on the *XY* plane. Although the device structure is symmetrical, the resonant frequencies of the first and second modes are not the same since the shape of the image sensor attached to the image stabilizer is not symmetrical. The typical frequency

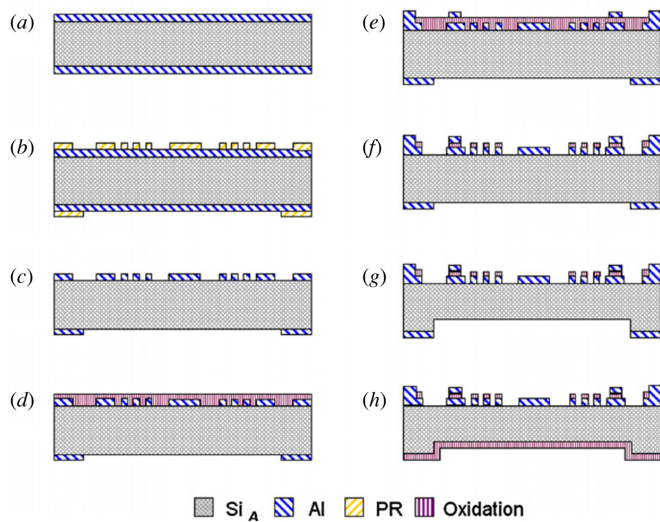

Figure 7. Fabrication process of the device layer of the image stabilizer. (*a*) Al deposition on both sides of Si, (*b*) definitions of the device and anchor layer by PR coating and lithography, (*c*) Al etching, (*d*) isolation layer formatting by SiO_2 PECVD deposition, (*e*) routing layer definition by Al deposition and etching, (*f*) ICP etching and contact windows opening by RIE, (*g*) anchor formation by first ICP etching and (*h*) SiO_2 deposition on the backside of the Si wafer.

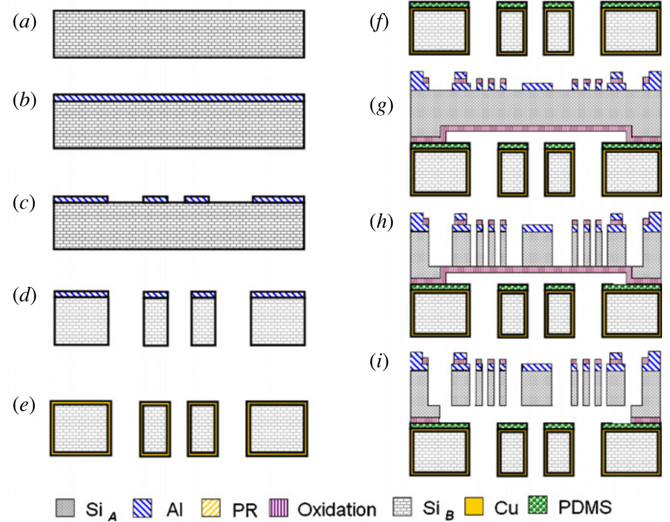

Figure 8. Fabrication process of an image stabilizer. (*a*) Si_B for the device holder, (*b*) Al deposition, (*c*) ICP hard mask definition by Al etching, (*d*) wafer punching-through by ICP etching, (*e*) Cu deposition by dc sputtering, (*f*) PDMS spin coating, (*g*) the device combination by flip-chip bonder, (*h*) the device formation by third ICP etching and (*i*) the device release by HF vapor.

of human hand jitter is in the range of 10–20 Hz [25, 26]. Thus, one must avoid operating frequencies that are close to this resonant frequency to ensure stability.

4. Fabrication

4.1. Processes for fabricating the structure layer and substrate holder

The structure, substrate holder and its parts are fabricated. Figure 7 shows the structure fabrication process. During structure fabrication, the structure definition, contact window opening, circuit routing and electrical isolation are completed. Fabrication begins with a 250 μm thick 1 0 0 silicon wafer. The following steps describe all the fabrication processes.

(a) During basic RCA cleaning, a thin 1 μm thick Al layer is deposited on the front and backsides of an Si wafer by dc sputtering (figure 7(*a*)).
(b) During photolithography, the device structure and anchor shape are patterned on the front and backsides of the Si wafer. On the front side of the Si wafer, the photoresist layer is patterned as the device structure layer in the Al etching process. On the backside of the Si wafer, the photoresist layer is patterned as the anchor shape layer for anchor hard-mask formation during Al etching (figure 7(*b*)).
(c) Via Al wet etching, Al on the front side of the Si wafer is patterned as the hard mask for the device structure during the second ICP etching process. Notably, Al on the backside of the Si wafer functions as the ICP hard mask during the first ICP etching process (figure 7(*c*)). This Al layer on the front side is reserved as the conductive layer after ICP etching.
(d) On the front side of the Si wafer, 1 μm SiO_2 is deposited to generate an isolation layer between the structure layer and circuit routing layer (figure 7(*d*)).
(e) After opening the contact windows by RIE etching, Al sputtering is executed again to pattern the circuit routing layer (figures 7(*e*), (*f*)).
(f) The first ICP etching process is performed to form an anchor shape on the backside of the Si wafer at a depth of 130 μm (figure 7(*g*)).
(g) Finally, 1 μm SiO_2 is deposited again on the backside of the Si wafer as the etching stop layer (figure 7(*h*)).

During substrate holder formation, the substrate holder is designed based on the wire bonding process. This holder is used to pass through these hollow areas to support the suspended device during the wire bonding process. Figure 8 shows the substrate holder fabrication and bonding process. Initially, Si_B is prepared for substrate holder fabrication and starts with the same RCA cleaning process as that applied to Si_A (figure 8(*a*)). A thin 8000 Å Al layer is then deposited by dc sputtering (figure 8(*b*)), and is lithographically patterned as the hard mask for the substrate structure fabrication during ICP etching (figure 8(*c*)). Next, this Si wafer is subjected to ICP etching until it is completely punched through (figure 8(*d*)) and Al is stripped by wet etching. To achieve etching uniformity during ICP etching, 1 μm Cu is sputtered on the front and backsides of Si_B to release heat during the ICP etching process (figure 8(*e*)).

The final step combines the device structure and substrate holder. This step is performed by flip-chip bonding, ICP etching and HF vapor methods. Figures 8(*f*)–(*i*) show the process of the final fabrication task. Initially, 20 μm thick polydimethylsiloxane (PDMS) is spun upon Si_B by a spinning coater (figure 8(*f*)). Next, Si_A and Si_B are combined by the flip-chip bonder and heated to 120 °C for 2 min

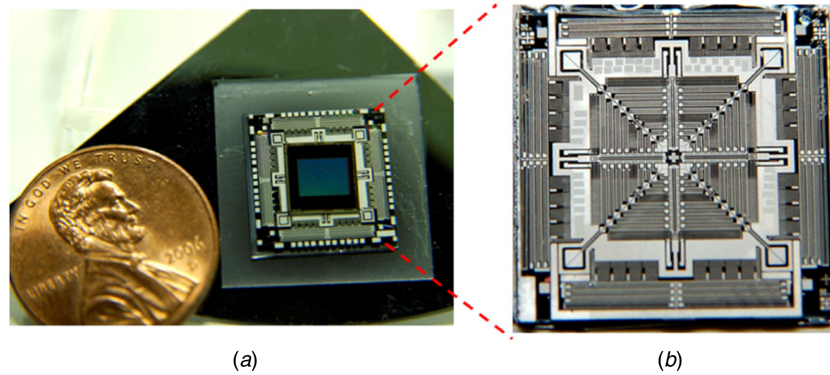

(*a*) (*b*)

Figure 9. Photographs of the image stabilizer.

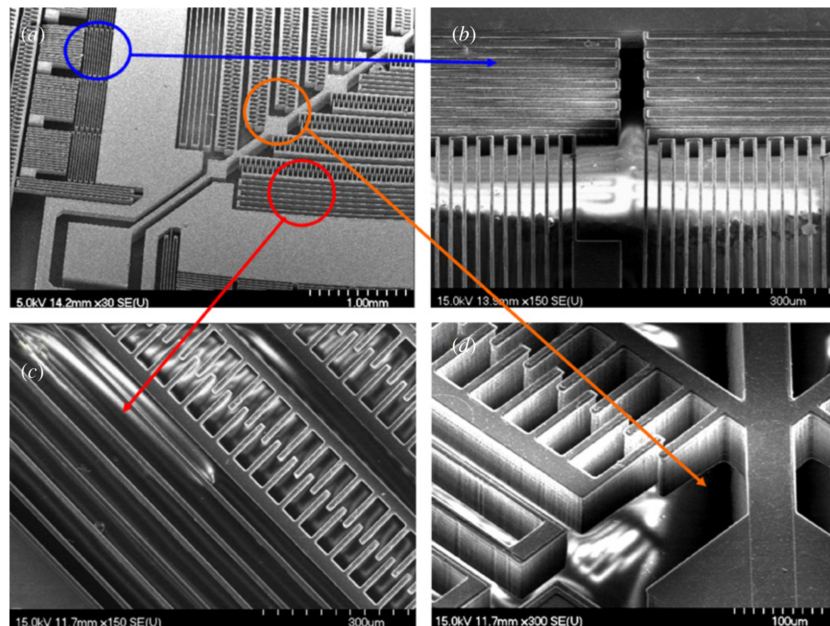

Figure 10. SEM pictures of a part of the image stabilizer: (*a*) suspended structure, (*b*) signal springs, (*c*) folded beams and (*d*) comb flingers and anchors.

(figure 8(*g*)). After the bonding process, the third ICP etching process is applied to fabricate the device structure, and is completed at the etching stop layer (figure 8(*h*)). The HF vapor etching technique is finally employed to release the device structure without any solution treatment. Device structures are released when the SiO_2 layer is etched by the HF vapor method. Additionally, the device-sticking problem is prevented during wet etching (figure 8(*i*)). Figures 9 and 10 show photographs and scanning electron microscope (SEM) micrographs of the fabricated image stabilizer. Figure 9(*a*) shows an image sensor attached to the proposed image stabilizer (without the wire bonding process). Figure 9(*b*) shows the entire image stabilizer. Figure 10 shows the SEM micrographs of the proposed suspended devices.

4.2. Wire bonding and device packaging

An image sensor is combined with the proposed image stabilizer using the flip-chip bonding process. Since the proposed image stabilizer is entirely suspended in midair, attaching the image sensor directly to the actuator is extremely difficult. Suspension springs of the decoupling *XY* stage are extremely fragile, and may break during wire bonding. To overcome this problem, a WBAH is designed to support device weight and resist bonding pressure during flip-chip and wire bonding. Figure 11 shows the flip-chip process for image sensor bonding and wire bonding packaging. The image sensor is bonded onto the proposed image stabilizer using a flip-chip bonder. First, the WBAH is attached under the proposed image stabilizer via flip-chip bonding. Due to the hollow design of the handle layer of the proposed image stabilizer, suspended structures are fully supported by the WBAH (figures 11(*a*) and (*b*)). Next, PDMS is utilized as an adhesive and via flip-chip bonding, the image sensor is attached to the image stabilizer and heat-treated at 120 °C for 10 min to ensure that the sensor and stabilizer are fully bonded (figure 11(*c*)). Following the wire bonding process and removal of the WBAH, the electrical connection between the image sensor and suspended device is completed as a special package. Figure 12 shows the packaging process captured by the flip-chip bonder monitor. Figures 12(*a*)–(*c*) show the image stabilizer combined with the WBAH. Figures 12(*d*)–(*f*)

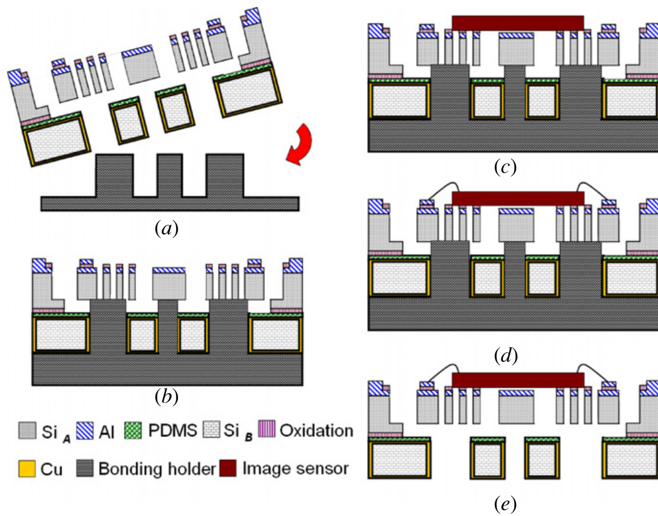

Figure 11. Package and wire bonding process of the image stabilizer.

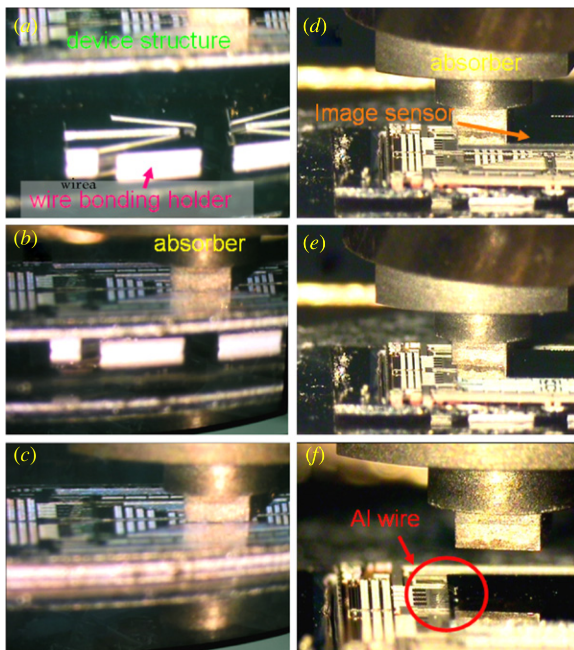

Figure 12. Photographs of the package and wire bonding process of the image stabilizer.

show the image stabilizer and image sensor combined using the flip-chip bonding and wire bonding processes. Figure 13 shows photographs and SEM micrographs of the packaged image stabilizer. The image stabilizer has the image sensor (figures 13(*a*) and (*b*)). Additionally, wire bonding is applied to achieve an electrical connection between the image sensor and signal output beams (figures 13(*c*) and (*d*)).

5. Results and discussion

The effectiveness of the 2D decoupled image stabilizer was assessed. During the static driving test, the actuator was driven by dc voltage. The actuator displacement was measured by

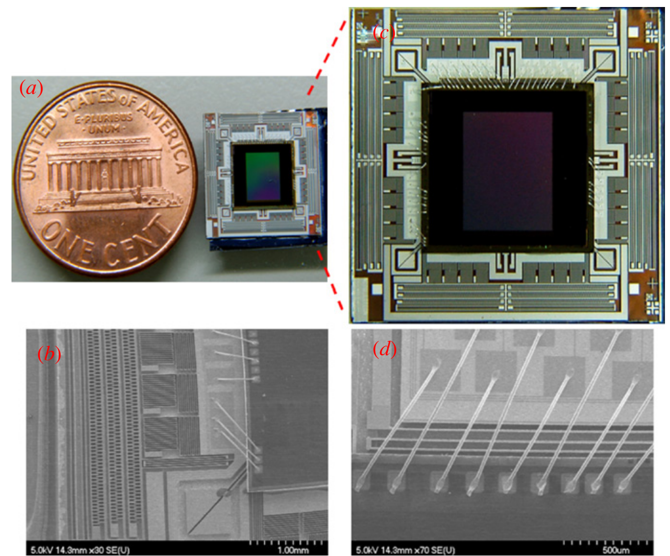

Figure 13. Photographs of the image stabilizer with the wire bonding package.

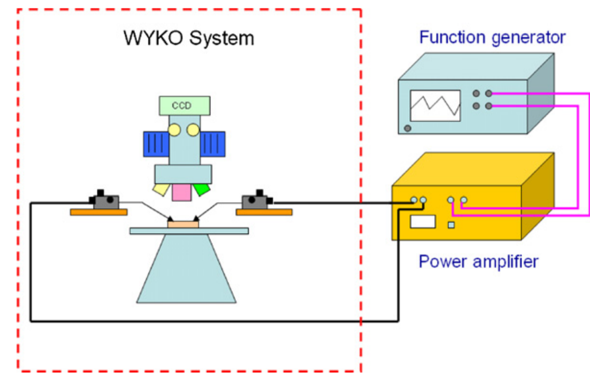

Figure 14. Illustration of the static measurement of the WYKO system.

a white light interferometer (WYKO) (figure 14). When a 51 V driving voltage was applied to the proposed device in the *x*-direction, the moving displacement in the *x*-direction was 25 μm and the displacement along the vertical *y*-axis was only 0.42 μm. When a 54 V driving voltage was applied to the proposed device in the *y*-direction, the moving displacement in the *y*-direction was 25 μm and the displacement along the vertical *x*-axis was only 0.34 μm. In the *x*-direction, the experimental decoupling ratio of the *x* displacement to the *y* displacement was 59.52, conforming to the system requirement that the decoupling ratio exceeds 11.1. In the *y*-direction, the experimental decoupling ratio of the *y* displacement to the *x* displacement was roughly 73.53, conforming to the system requirement that the decoupling ratio exceeds 11.1. Figure 15 presents displacement variation with driving voltage. In the dynamic characterization, a MEMS motion analyzer (MMA) system is set up to evaluate the resonant frequency of the proposed image stabilizer. Figure 16 plots the measurements as resonance frequency reaches 1.123 kHz. Experimental results indicate that the resonance frequency is 2.1% lower than the simulated first natural frequency of 1.123 kHz. This discrepancy is caused by

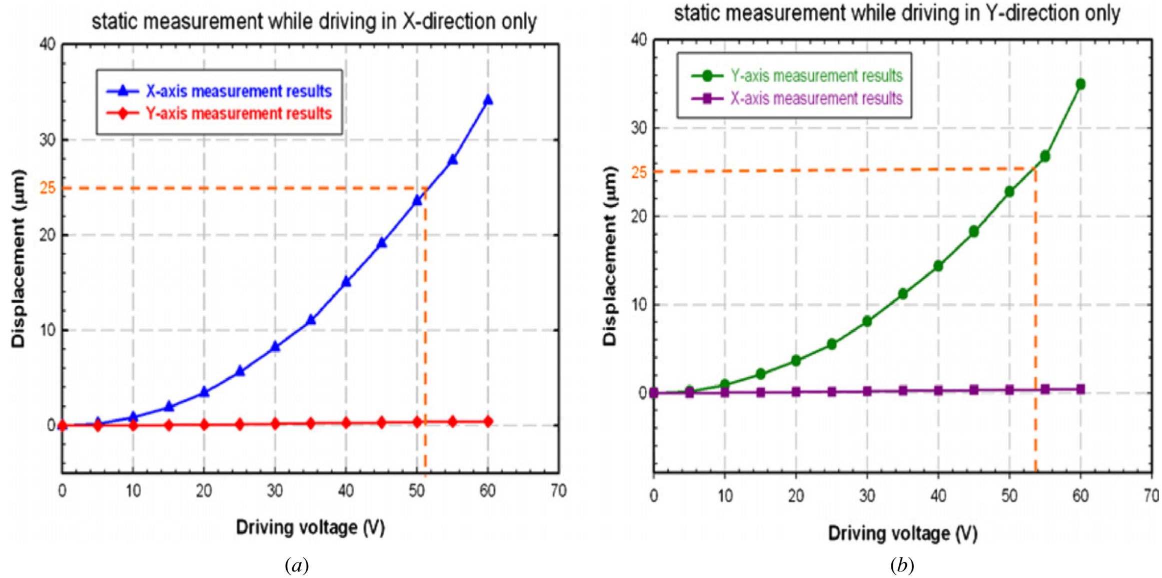

Figure 15. Static measurement of the *XY* stage in the *X*- and *Y*-directions when driven in (*a*) the *X*-direction only and (*b*) the *Y*-direction.

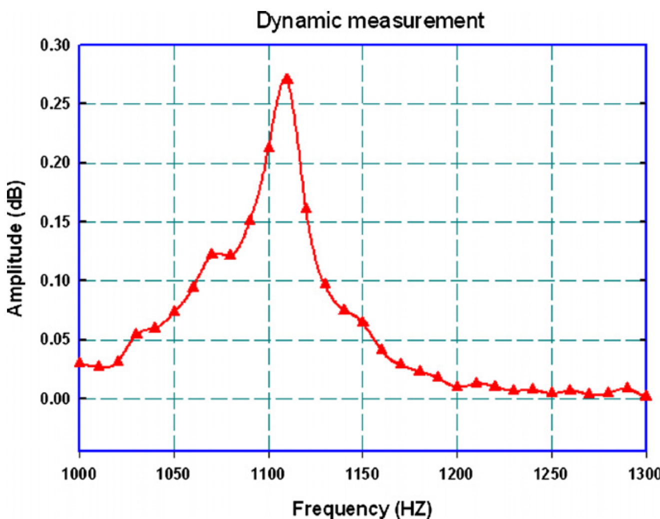

Figure 16. Measurement results of the resonant frequency.

the inaccuracy of the fabrication process and weight variation of the image sensor. Furthermore, the simulation model does not consider the weight of PDMS, possibly causing some difference in the simulated and actual weight.

6. Conclusion

This work designs, simulates and fabricates a novel integrated micro decoupling *XY* stage. This integrated *XY* stage is designed to support a three-megapixel image sensor. Based on the design of the WBAH, the image sensor can be successfully bonded to the image stabilizer. Additionally, electrical signals of the image sensor can be connected and integrated with the output circuits based on the signal spring design. This image stabilizer can be utilized by commercially available cell phone cameras to provide an anti-shaking function. The proposed device is primarily composed of a silicon-based *XY* stage, a comb actuator, which is fabricated and packaged via three ICP etching processes, the flip-chip bonding technique and a unique wire bonding method. Experimental results demonstrate that a driving voltage of 51 V can cause a displacement of 25 μm in the driving direction and a displacement of 0.42 μm in the vertical direction, both of which are consistent with the anti-shaking goal. Similar experimental results apply to the perpendicular direction because of the symmetrical design of the proposed structure. The difference between simulation and experimental results is caused by the undercutting of comb fingers that occurs during the ICP etching process and by neglecting the weight of the small amount of PDMS. The natural frequency of the proposed *XY* stage is measured at 1.123 kHz using the MMA system.

Acknowledgments

This work was partially supported by the Lite-On Technology Corporation and the National Science Counsel under contract nos NSC 97-2220-E-009-026 and NSC97-2220-E-009-044. The authors would also like to thank Rigid-tech Technology Corporation for technical support.

References

[1] Sun L, Wang J, Rong W, Li X and Bao H 2008 A silicon integrated micro nano-positioning *XY*-stage for nano-manipulation *J. Micromech. Microeng.* **18** 125004
[2] Takahashi K, Mita M, Fujita H and Toshiyoshi H 2006 A high fill-factor comb-driven *XY*-stage with topological layer switch architecture *IEICE Electron. Express* **3** 197–202
[3] Kwon H N, Lee J-H, Takahashi K and Toshiyoshi H 2006 Micro *XY* stages with spider-leg actuators for two-dimensional optical scanning *Sensors Actuators* A **130–131** 468–77
[4] Kwon S and Lee L P 2002 Stacked two dimensional micro-lens scanner for micro confocal imaging array *Proc. IEEE MEMS '02* pp 483–6

[5] Laszczyk K, Bargiel S, Gorecki C and Krezel J 2008 Towards integration of glass microlens with silicon comb-drive *X-Y* microstage *IEEE/LEOS Int. Conf. on Optical MEMS and Nanophotonics* pp 168–9
[6] Yasumura K Y, Grade J D and Jerman H 2002 Fluid damping of an electrostatic actuator for optical switching applications *Proc. Solid-State Sensor, Actuator and Microsystems Workshop* pp 358–61
[7] Takahashi K, Kwon H N, Mita M, Saruta K, Lee J-H, Fujita H and Toshiyoshi H 2007 A silicon micromachined f-θ microlens scanner array by double-deck device design technique *IEEE J. Sel. Top. Quantum Electron.* **13** 277–82
[8] Yang J P, Mou J Q, Chong N B, Lu Y, Zhu H, Jiang Q, Kim W G, Chen J, Guo G X and Ong E H 2007 Probe recording technology using novel MEMS devices *Microsyst. Technol.* **13** 733–40
[9] Ando Y 2004 Development of three-dimensional electrostatic stages for scanning probe microscope *Sensors Actuators* A **114** 285–91
[10] Indermuhle P F, Linder C, Brugger J, Jaecklin V P and de Rooij N F 1994 Design and fabrication of an overhanging *XY*-microactuator with integrated tip for scanning surface profiling *Sensors Actuators* **43** 346–50
[11] Kawai Y, Ono T, Esashi M, Meyer E and Gerber C 2007 Resonator combined with a piezoelectric actuator for chemical analysis by force microscopy *Rev. Sci. Instrum.* **78** 063709
[12] Kim C H, Jeong H M, Jeon J U and Kim Y K 2003 Silicon micro *XY*-stage with a large area shuttle and no-etching holes for SPM-based data storage *J. Microelectromech. Syst.* **12** 470–8
[13] Lu M S-C and Fedder G K 2004 Position control of parallel-plate microactuators for probe-based data storage *J. Microelectromech. Syst.* **13** 759–69
[14] Liu X, Kim K and Sun Y 2007 A MEMS stage for 3-axis nanopositioning *J. Micromech. Microeng.* **17** 1796–802
[15] Mukhopadhyay D, Dong J, Pengwang E and Ferreira P M 2008 A SOI MEMS based 3-DOF planar parallel-kinematics nanopositioning stage *Sensors Actuators* A **147** 340–51
[16] Gu L, Li X, Bao H, Liu B, Wang Y, Liu M, Yang Z and Cheng B 2006 Single-wafer-processed nano-positioning *XY*-stages with trench-sidewall micromachining technology *J. Micromech. Microeng.* **16** 1349–57
[17] Yeom D H, Park N J and Jung S Y 2007 Digital controller of novel voice coil motor actuator for optical image stabilizer *Int. Conf. on Control, Automation and Systems* pp 2201–6
[18] Sato K, Ishizuka S, Nikami A and Sato M 2005 Control techniques for optical image stabilizing system *IEEE Trans. Consum. Electron.* **39** 461–6
[19] Okamoto Y and Yoshida R 1998 Development of linear actuators using piezoelectric elements *Electron. Commun. Japan* III **81** 11–7
[20] Chen G-R, Yeh Y-M, Wang S-J and Chiang H-C 2000 A novel structure for digital image stabilizer *IEEE Asia-Pacific Conf. on Circuits and Systems* pp 101–4
[21] Mohamed A, Elsimar H and Ismail M 2003 Analysis and optimization of a CMOS vertical thermal actuator *Proc. Symp. Design, Test, Integration and Packaging of MEMS/MOEMS* pp 214–7
[22] Alper S E and Akin T 2005 A single-crystal silicon symmetrical and decoupled MEMS gyroscope on an insulating substrate *J. Microelectromech. Syst.* **14** 707–17
[23] Tang W C, Nguyen T-C H and Howe R T 1989 Laterally driven polysilicon resonant microstructures *Proc. IEEE Micro Electro Mechanical Systems* pp 53–9
[24] Legtenberg R, Groeneveld A W and Elwenspoek M 1996 Comb-drive actuators for large displacements *J. Micromech. Microeng.* **6** 320–9
[25] Sachs D, Nasiri S and Goehl D Image stabilization technology overview http://www.invensense.com/shared/pdf/ImageStabilizationWhitepaper_051606.pdf
[26] Song M-G *et al* 2009 Development of small sized actuator for optical image stabilization *Int. Symp. on Optomechatronic Technologies (21–23 September 2009)* pp 152–7